Neutron powder diffraction study of the ferroelastic phase transition and lattice melting in sodium carbonate, Na_2CO_3

1995 J. Phys.: Condens. Matter 7 4395

(http://iopscience.iop.org/0953-8984/7/23/010)

J. Phys.: Condens. Matter 7 (1995) 4395–4417. Printed in the UK

Neutron powder diffraction study of the ferroelastic phase transition and lattice melting in sodium carbonate, Na_2CO_3

Ian P Swainson†, Martin T Dove†‡ and Mark J Harris§‖

† Neutron and Condensed Matter Science Branch, AECL Research, Chalk River Laboratories, Chalk River, Ontario K0J 1J0, Canada

‡ Mineral Physics Group, Department of Earth Sciences, University of Cambridge, Downing Street, Cambridge CB2 3EQ, UK

§ Oxford Physics, Clarendon Laboratory, Parks Road, Oxford OX1 3PU, UK

Received 13 March 1995

Abstract. Detailed neutron powder diffraction data are presented which show that the phase transition ($P6_3/mmc$–$C2/m$) at 754 K in sodium carbonate, Na_2CO_3, is a second-order proper ferroelastic $m = 2$ transition. The order parameter is characterized by the shear strain ϵ_5, with a coupled rotation of the carbonate groups. The diffraction peaks show clear evidence for the divergence of the temperature factors at the transition temperature due to the softening of the acoustic modes at small wave vectors. This results in the appearance of broad diffuse scattering at Bragg positions at the expense of the intensities of the Bragg peaks. We call this process 'lattice melting'.

1. Introduction

Sodium carbonate, Na_2CO_3, has been studied in some detail recently because of the important incommensurate phase transition at 633 K [1, 2]. Less attention has been paid to the hexagonal–monoclinic phase transition at ~760 K. The symmetry change from $P6_3/mmc$ to $C2/m$, with no change in the size of the primitive cell, suggests that the phase transition is a proper ferroelastic transition with a two-dimensional order parameter [3, 4]. The dimension of the order parameter is important, since it defines a distinct class of ferroelastic materials. A Guinier–Lenné x-ray powder diffraction photograph shown by De Wolff and Tuinstra [1] suggests that the transition in Na_2CO_3 might be second order. There are only a few well characterized examples of this class of ferroelastic material, such as KCN and KCN:KBr mixtures, and $KAlF_4$, and there are apparently no other known examples of pure systems where this type of phase transition is second order. In the light of recent theoretical work on second-order phase transitions of this type [5], it is clear that detailed crystallographic studies of a number of such systems are needed. Thus we report here a study of the hexagonal–monoclinic phase transition in sodium carbonate using high-resolution neutron powder diffraction, and address two issues. Firstly, we are interested in the characterization of the transition—for example, what is the *primary* instability, and is the transition really second order? Secondly, we are interested in the effects of the phase transition on the shapes of the Bragg peaks and crystallographic temperature factors, following the recent theoretical analysis of Mayer and Cowley [5] appropriate for this type of material. In this latter regard, we believe that the results we will present below are among the most striking phenomena found in any ferroelastic material.

‖ Present address: ISIS Facility, Rutherford Appleton Laboratory, Chilton, Didcot, Oxfordshire OX11 0QX, UK.

0953-8984/95/234395+23$19.50

Table 1. Representations of the atomic coordinates in the β- and α-phases of sodium carbonate. The coordinates correspond to the usual settings of the two space groups.

β-phase ($C2/m$)		α-phase ($P6_3/mmc$)	
Na(1)	$0, 0, 0$	Na(I)	$0, 0, 0$
Na(2)	$0, 0, \frac{1}{2}$	(Na(I)	$0, 0, \frac{1}{2}$)
Na(3)	$x, \frac{1}{2}, z$	Na(II)	$\frac{2}{3}, \frac{1}{3}, \frac{3}{4}$
C	$x, \frac{1}{2}, z$	C	$\frac{2}{3}, \frac{1}{3}, \frac{1}{4}$
O(1)	x, y, z	O	$x, -x, \frac{1}{4}$
O(2)	$x, \frac{1}{2}, z$	(O	$x + y, \frac{1}{2}, \frac{1}{4}$)

The crystal structure of the high-temperature hexagonal α-phase of sodium carbonate is represented in figure 1. One of the sodium atoms, Na(I), is octahedrally coordinated to the oxygen atoms, and the NaO_6 octahedra form face sharing columns along [001]. The columns are interconnected by the oxygen atoms which are shared with the carbonate groups. The second sodium atom, Na(II), is located in a larger site above the carbon atoms. The crystal structure of the low-temperature monoclinic β-phase is shown in figure 1(*d*). The individual columns of NaO_6 octahedra do not distort significantly as a result of the α–β phase transition, but neighbouring columns move along [001] with respect to each other on cooling through the transition, hinged by the carbonate groups which rotate in phase with the shear strain. The sodium atoms Na(1) and Na(2), which are symmetrically distinct in the monoclinic structure, are related to Na(I) in the hexagonal phase, and Na(3) is related to Na(II). The two oxygen atoms O(1) and O(2) are equivalent in the hexagonal phase. The relationship between the atomic coordinates of both phases is summarized in table 1. The structure of the β-phase has previously been measured at only three temperatures, but our new measurements indicate that there are no other significant changes that occur through the phase transition.

The active representation for the change of symmetry in the hexagonal–monoclinic phase transition is the two-dimensional representation E_{1g}. One of the two components of this generates the $C2/m$ monoclinic structure found in sodium carbonate, this operation being characterized by the shear strain ϵ_5, whereas the other generates a different monoclinic structure of space group $C2/c$, as found in potassium carbonate, K_2CO_3 [1]. The symmetry allows for a second-order phase transition in the sense of Landau theory [4]. The results presented below show that there is no measureable first-order discontinuity in Na_2CO_3, and that the phase transition can be described by a Landau free energy. The transition can be generated by softening of the C_{44} elastic constant, which leads to the softening of all the transverse acoustic modes that have wave vectors in the a^*–b^* plane and eigenvectors polarized along [001]. This softening of the acoustic modes over a two-dimensional sector of reciprocal space defines a distinct class of ferroelastic phase transitions, denoted as $m = 2$ by Folk *et al* [6, 7], which is different from the more common case where the acoustic modes only soften along certain directions in reciprocal space ($m = 1$).

The results we present in this paper show that sodium carbonate is a particularly good example for the study of phenomena associated with second-order $m = 2$ ferroelastic phase transitions. In particular we are interested in the prediction of logarithmic divergence of the temperature factors (equivalent to the mean squared atomic displacements) that arises from the softening of the acoustic modes for wave vectors in a plane in reciprocal space [5, 6, 7]. This causes a complete loss of long-range order at the transition temperature, and a subsequent vanishing of the intensities of the Bragg peaks. Since the divergence of

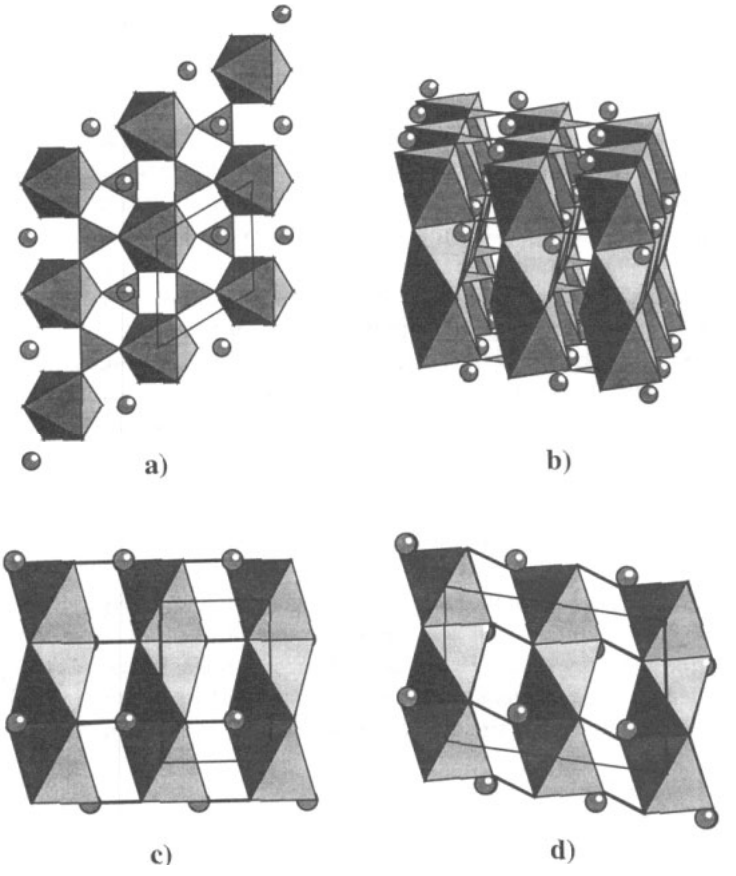

Figure 1. (*a*) Plan of the structure of the hexagonal α-phase of sodium carbonate viewed down [001], showing the $Na(I)O_6$ octahedra and the carbonate groups (triangles). The position of the Na(II) atom is directly above the carbon atom, and is indicated by the shaded sphere. (*b*) Perspective view of the structure of the hexagonal α-phase of sodium carbonate, showing the carbonate groups (triangles) acting as hinges connecting the columns of face sharing $Na(I)O_6$ octahedra. (*c*) Plan of the structure of the hexagonal α-phase of sodium carbonate viewed down [010], for comparison with (*d*). The thick lines indicate the planes of the carbonate groups. (*d*) Plan of the structure of the monoclinic β-phase of sodium carbonate viewed down [010]. In this projection the shear strain and the coupled hinged rotations of the carbonate groups are clear, particularly when compared with the view of the hexagonal phase from the same direction, (*c*).

the temperature factors is due to the acoustic modes, which cause neighbouring atoms to be displaced in phase by the same distance, some degree of short-range order is preserved. The loss of long-range order at the transition temperature has some similarities to melting [5], but unlike real melting long-range order is recovered both by heating above and by cooling below the transition temperature. Moreover, there is no large change in the local order nor is there significant atomic diffusion. In effect, the melting is associated with the lattice rather than with the atomic order, and therefore we have called this effect 'lattice melting' [8]. Mayer and Cowley [5] have shown that at the transition temperature the Bragg peaks are replaced by broad peaks of diffuse scattering, and they have derived an expression for the shape of these peaks at the transition temperature. On approaching the

transition temperature the Bragg peaks will decrease in intensity and the peaks of diffuse scattering will increase. Something like lattice melting has been observed in the mixed system KCN:KBr [9], but in this case the random defects prevent the complete loss of the Bragg peak intensities [10]. Preliminary neutron powder diffraction measurements of the corresponding $m = 2$ transition in K_2CO_3 have been made recently at Chalk River and indicate that lattice melting occurs in this material as well. As far as we are aware all other known examples of $m = 2$ ferroelastic phase transitions are first order, and in these cases the effects of lattice melting are unlikely to be observed. Thus Na_2CO_3 is an ideal system for the study of lattice melting.

The rest of the paper takes the following form. In section 2 we outline some theoretical points concerning the scattering in the presence of lattice melting. In section 3 we describe our experimental work. In sections 4 and 5 we describe and discuss the crystallographic aspects of the phase transition. Finally in section 6 we consider in some detail the phenomenon of lattice melting by analysing the temperature dependence of the profiles of the diffraction peaks.

2. Some comments on the neutron scattering law and lattice melting

The lattice melting phenomenon outlined above involves the divergence of the temperature factor due to the softening of an acoustic mode over a plane of wave vectors. This leads to a loss of the intensity of the Bragg peak, which is replaced by a broad peak of diffuse scattering. Denoting the intensities of the Bragg and diffuse scattering peaks by I_{Bragg} and I_{Diffuse} respectively, we can write the total scattering I_{Total} as a sum of these two terms:

$$I_{\text{Total}} = I_{\text{Bragg}} + I_{\text{Diffuse}}. \tag{1}$$

In a diffraction experiment the measured quantity, I_{Total}, is the total scattering integrated over all energies, whereas the Bragg component is a delta function at zero energy. Both terms are written as

$$I_{\text{Total}} = \left\langle \left| \sum_j b_j \exp\left(\mathrm{i}\boldsymbol{Q} \cdot \boldsymbol{r}_j\right) \right|^2 \right\rangle \tag{2}$$

$$I_{\text{Bragg}} = \left| \left\langle \sum_j b_j \exp\left(\mathrm{i}\boldsymbol{Q} \cdot \boldsymbol{r}_j\right) \right\rangle \right|^2 \tag{3}$$

where $\boldsymbol{r}_j$ is the position of the jth atom (assumed to vary with time), b_j is the corresponding neutron scattering length, and Q is the scattering vector. We have neglected factors that depend on geometry and scale factors. We can write the instantaneous position of an atom as

$$\boldsymbol{r} = \boldsymbol{R} + \boldsymbol{u}^{\mathrm{O}} + \boldsymbol{u}^{\mathrm{A}} \tag{4}$$

where R is the average position, $\boldsymbol{u}^{\mathrm{O}}$ is the displacement due to all the phonons except the soft acoustic modes, and $\boldsymbol{u}^{\mathrm{A}}$ is the displacement due to the soft acoustic modes. Thus we can rewrite the expression for the total intensity as

$$I_{\text{Total}} = \left\langle \left| \sum_j b_j \exp\left(\mathrm{i}\boldsymbol{Q} \cdot \left[\boldsymbol{R}_j + \boldsymbol{u}_j^{\mathrm{O}} + \boldsymbol{u}_j^{\mathrm{A}}\right]\right) \right|^2 \right\rangle \tag{5}$$

that is

$$I_{\text{Total}} = \left\langle \sum_{i,j} b_i b_j \exp\left(\mathrm{i}\boldsymbol{Q}\cdot\left[\boldsymbol{R}_i - \boldsymbol{R}_j\right]\right) \exp\left(\mathrm{i}\boldsymbol{Q}\cdot\left[\boldsymbol{u}_i^{\mathrm{O}} - \boldsymbol{u}_j^{\mathrm{O}}\right]\right) \exp\left(\mathrm{i}\boldsymbol{Q}\cdot\left[\boldsymbol{u}_i^{\mathrm{A}} - \boldsymbol{u}_j^{\mathrm{A}}\right]\right) \right\rangle \quad (6)$$

which approximates to

$$I_{\text{Total}} \simeq \sum_{i,j} b_i b_j \exp\left(\mathrm{i}\boldsymbol{Q}\cdot\left[\boldsymbol{R}_i - \boldsymbol{R}_j\right]\right) \left\langle \exp\left(\mathrm{i}\boldsymbol{Q}\cdot\left[\boldsymbol{u}_i^{\mathrm{O}} - \boldsymbol{u}_j^{\mathrm{O}}\right]\right)\right\rangle \left\langle \exp\left(\mathrm{i}\boldsymbol{Q}\cdot\left[\boldsymbol{u}_i^{\mathrm{A}} - \boldsymbol{u}_j^{\mathrm{A}}\right]\right)\right\rangle \quad (7)$$

where we assume a decoupling of the effects of the soft acoustic modes (the critical modes) and the effects of all other phonons (the non-critical modes). We note that within the harmonic approximation we can now separate out the non-critical terms:

$$I_{\text{Total}} = \sum_{i,j} b_i b_j \exp\left(\mathrm{i}\boldsymbol{Q}\cdot\left[\boldsymbol{R}_i - \boldsymbol{R}_j\right]\right) \exp\left(-\left[W_i^{\mathrm{O}}(\boldsymbol{Q}) + W_j^{\mathrm{O}}(\boldsymbol{Q})\right]\right) \left\langle \exp\left(\mathrm{i}\boldsymbol{Q}\cdot\left[\boldsymbol{u}_i^{\mathrm{A}} - \boldsymbol{u}_j^{\mathrm{A}}\right]\right)\right\rangle \quad (8)$$

where we have defined the non-critical contribution to the temperature factor

$$W_j^{\mathrm{O}}(\boldsymbol{Q}) = \frac{1}{2}\left\langle \left(\boldsymbol{Q}\cdot\boldsymbol{u}_j^{\mathrm{O}}\right)^2 \right\rangle. \quad (9)$$

In deriving the above expression we have also assumed that the inelastic scattering from the displacements $\boldsymbol{u}^{\mathrm{O}}$ does not contribute significantly to the total scattering. This assumption is not valid for the critical displacements $\boldsymbol{u}^{\mathrm{A}}$.

We proceed with a plausibility argument. The Bragg term is given as

$$I_{\text{Bragg}} = \left| \sum_j b_j \exp\left(i\boldsymbol{Q}\cdot\boldsymbol{R}_j\right) \exp\left(-W_j^{\mathrm{O}}(\boldsymbol{Q})\right) \exp\left(-W_j^{\mathrm{A}}(\boldsymbol{Q})\right) \right|^2 \quad (10)$$

where

$$W_j^{\mathrm{A}}(\boldsymbol{Q}) = \frac{1}{2}\left\langle \left(\boldsymbol{Q}\cdot\boldsymbol{u}_j^{\mathrm{A}}\right)^2 \right\rangle \quad (11)$$

As we have noted above, on approaching T_c the displacements $\boldsymbol{u}^{\mathrm{A}}$ diverge, so that the factor $\exp(-W_j^{\mathrm{A}}(\boldsymbol{Q}))$ and hence I_{Bragg} fall to zero. Since $\boldsymbol{u}^{\mathrm{A}}$ is determined by the long-wavelength acoustic modes, $W_j^{\mathrm{A}}(\boldsymbol{Q})$ will be the same for each atom in the unit cell. Moreover, we expect that the quantity $\boldsymbol{u}_i^{\mathrm{A}} - \boldsymbol{u}_j^{\mathrm{A}}$ will be close to zero for atoms separated over quite large distances. Therefore we expect that $< \exp(\mathrm{i}\boldsymbol{Q}\cdot[\boldsymbol{u}_i^{\mathrm{A}} - \boldsymbol{u}_j^{\mathrm{A}}]) > \simeq 1$ for all pairs of atoms, so that the total scattering intensity can be approximated as

$$I_{\text{Total}} \simeq \sum_{i,j} b_i b_j \exp\left(\mathrm{i}\boldsymbol{Q}\cdot\left[\boldsymbol{R}_i - \boldsymbol{R}_j\right]\right) \exp\left(-\left[W_i^{\mathrm{O}}(\boldsymbol{Q}) + W_j^{\mathrm{O}}(\boldsymbol{Q})\right]\right). \quad (12)$$

Implicit in the argument is the integration over all values of $\mathbf{Q}$ in the vicinity of each Bragg peak, which is justified if, as in the present case, the width of the scattering is small in comparison with the size of the reciprocal lattice parameters. From our argument we expect that although the Bragg intensity falls to zero as the critical displacements diverge, the total intensity is unaffected—the intensity of the diffuse scattering term increases to compensate for the loss of Bragg scattering. This tentative conclusion is supported by the data we present below, although we recognise that our arguments do not constitute a proof of this point. (Mikeska and Schmidt [11] claim that this result is exact, by deriving an expression for the scattering intensity $I(\boldsymbol{Q})$ of a two-dimensional crystal and inviting the reader to verify that the total intensity is constant by integration of $I(\boldsymbol{Q})$ over the region around $\boldsymbol{Q}$.) The difference between the total scattering and the Bragg scattering is that the total scattering

takes account of the correlation between the critical displacements, whereas the Bragg term assumes no correlation. These arguments suggest that there is complementary structural information in the total and Bragg intensities. If the total scattering were analysed as if it were Bragg scattering, it would yield the same information about the atomic positions as would be obtained from the analysis of the Bragg intensities, expect that the refined temperature factors would be those associated with the non-critical atomic displacements, u_j^O, rather than the total displacements, $u_j^O + u_j^A$. This is the approach we have taken in our Rietveld analysis below. The critical displacements can then be extracted simply as

$$W^A(Q) = -\frac{1}{2}\ln\left(\frac{I_{\text{Bragg}}}{I_{\text{Total}}}\right). \tag{13}$$

3. Experimental details

3.1. Neutron powder diffraction experiments

Our neutron powder diffraction measurements were obtained using the HRPD diffractometer at the ISIS spallation neutron source (Rutherford Appleton Laboratory, UK) and the C2 DUALSPEC diffractometer at the NRU reactor at Chalk River Laboratories (AECL Research, Canada).

HRPD is a high-resolution time of flight powder diffractometer [12]. Data were collected for flight times between 35 and 120 ms, corresponding to d spacings between ~0.7 and 2.4 Å. The sample was held in a vanadium can of diameter 10 mm. The furnace used for these measurements had a cylindrical vanadium heater that surrounded the sample. Temperatures were measured using a Chromel-A thermocouple. Measurements were obtained over the temperature range 5 to 1000 K, but in this paper we are only concerned with the measurements above 600 K. Partly because of problems with the temperature calibration on the furnace on HRPD, we did not obtain a complete set of data around the α–β phase transition temperature, which is why we then obtained a new set of data on the C2 diffractometer.

The C2 diffractometer is a high-resolution constant-wavelength powder diffractometer with an 800-wire curved detector covering an angular range of 80° [13]. For these experiments a wavelength of 1.505 53 Å was selected using an Si(5 3 1) monochromator, and its value was determined using a standard powder sample of silicon. For the majority of runs we collected data for scattering angles between 30 and 110° with two positions of the detector separated by 0.05°. For some runs however we collected data for scattering angles between 5 and 120° with points separated by 0.05° by using four positions of the detector. The sample was held in a vanadium can of diameter 8 mm. The furnace used for these measurements had a cylindrical graphite heater that surrounded the sample in the scattering plane. A diffraction peak from the furnace at ~25° was observed in the diffraction patterns and excluded from the profile refinements. Temperature was measured using a Chromel-A thermocouple. Measurements were obtained over the temperature range 605 to 970 K.

The width of a Bragg peak in the absence of any anomalous broadening is due to two factors: instrumental resolution, and sample properties such as particle size and internal strains—these define an effective resolution function for the measurements. Analysis of the (2 0 2) peak at high temperatures showed that the effective resolution function for this peak has a width of $\Delta d/d$ of 0.003 for HRPD and 0.007 for C2.

We used the same source material for the samples for the work on both diffractometers (99.995% purity, obtained from Aldrich Chemicals, UK). We used a fresh batch of material for each experiment, and the samples were dried thoroughly immediately before use.

3.2. Temperature control

Due to the large scale of the sample environment equipment in a neutron diffraction experiment, accurate measurements of the temperature are difficult, so a note on this detail is of some value. We used two thermocouples in the C2 furnace. The thermocouple used for temperature control was located close to the sample but not in contact with the sample or sample mount. A second thermocouple was used to read the temperature, and was attached to the sample at the position at which it was mounted onto the furnace. Typically we found that the temperature on this second thermocouple gave measurements that were 15–20 K lower than those given by the control thermocouple, and may be slightly lower than the real sample temperature because of heat losses. The transition temperature determined from measurements on heating on C2 was 754 K. This is within the range of temperatures for the transition measured by calorimetric methods [1], but lower than the value of 763 K preferred by other workers [14]. Given that a range of values of the transition temperature have been reported, we continue to use the value of 754 K here. Measurements were also obtained on cooling, and we found that there was a lag of 5 K on the temperature readings for the data of cooling below the transition temperature, as determined by comparing cell parameters. We therefore corrected the measured temperatures for these data sets by a simple constant addition of 5 K. The temperatures measured in the HRPD experiments were not consistent with those measured in the C2 data, so we calibrated the HRPD temperature measurements by comparing the unit cell angle β obtained from the structure refinements of the data from both HRPD and C2. The calibration simply required subtracting a small constant value from the measured temperatures.

4. Structure analysis

4.1. Analysis method and structure refinements

The data reduction for both instruments was carried out using the GENIE graphics program [15] with special routines written by the HRPD instrument scientists and ourselves.

The structure analysis was performed using the Rietveld refinement method with the program REFINE [16], which is based on the CCSL library [17]. As we have discussed in section 2, we have used the total peaks (the sum of the Bragg and diffuse scattering peaks) rather than only the Bragg peaks in our Rietveld analysis, and we recall our comment that we expect this to give the same structural information as we would get from analysis of the Bragg peaks alone, except that the temperature factors will be those due only to the non-critical phonon modes. The problem with using the total peaks is that the profiles of the peaks are not simply described by the resolution function, and we expect to see an $(h\,k\,\ell)$-dependent broadening. This turned out not to be a severe problem, since the broadening of the peaks due to the diffuse scattering is only significant at temperatures within a few degrees of the transition temperature: the widths of the diffuse peaks were not very much larger than the resolution function and were absorbed into the adjustable lineshape parameters. We do not expect this broadening to have any effect on the fitted values of the cell parameters, although there might be some residual effect on the fitted values of the atomic coordinates and temperature factors. Anticipating the results presented below, we found that at temperatures close to the transition temperature the refined values of the temperature factors became very large. In the refinements of the total scattering, these are the non-critical contributions to the total temperature factor in the sense of equation (9), which are not *a priori* expected to diverge as a result of the lattice melting. Nevertheless,

Table 2. Refined values of the unit cell parameters for the monoclinic β-phase (space group $C2/m$). The data obtained from C2 are shown in the upper section of the table, and the data from HRPD are shown in the lower section. The errors on the determination of the lattice parameters are of the order of 6×10^{-4} Å at 605 K rising to 2×10^{-3} Å close to T_c. Corresponding errors in β range from 4×10^{-3}° to 2×10^{-2}° as $T \rightarrow T_c$.

T (K)	a (Å)	b (Å)	c (Å)	β (deg)
605	8.97605	5.25081	6.21057	99.327
625	8.98459	5.25126	6.23259	98.870
645	8.99247	5.24709	6.26124	98.274
664	8.99881	5.24381	6.28680	97.689
684	9.00640	5.23793	6.31374	96.973
699	9.01120	5.23095	6.34223	96.193
703	9.01029	5.23116	6.34548	96.062
718	9.01203	5.22304	6.37509	95.167
723	9.01767	5.22534	6.37978	94.927
737	9.01516	5.20907	6.40528	93.705
741	9.02221	5.21862	6.42290	93.133
746	9.01791	5.21335	6.42992	92.574
749	9.01140	5.20590	6.43132	92.075
751	9.01859	5.20628	6.44172	91.603
611	8.98611	5.25645	6.22028	99.178
655	9.00289	5.24865	6.28012	97.951
673	9.01024	5.24430	6.30535	97.349
699	9.01852	5.23568	6.34912	96.184
743	9.03036	5.21574	6.43777	92.631

we found that these temperature factors did become very large, and as a consequence the fitted values of the atomic fractional coordinates will not be of high accuracy.

The background in the spectra, which was always strong compared to the signal, was represented by a Chebychev polynomial with fitted parameters. We assumed Gaussian line shapes with the standard U, V, W description of the angular dependence of the peak widths [18], noting that the parameters U, V, W will be affected by the broadening due to lattice melting.

The results of the structure refinements are given in tables 2–4. The structures obtained from the refinements of our data obtained at the lowest and highest temperatures are shown in figure 1.

4.2. Spontaneous strains and the order parameter

The temperature dependences of the unit cell parameters are shown in figure 2, and the data are given in table 2. These data were analysed by defining the following spontaneous strain components:

$$\epsilon_1 = \frac{a \sin \beta^*}{a_0} - 1 \tag{14}$$

$$\epsilon_2 = \frac{b}{b_0} - 1 \tag{15}$$

$$\epsilon_3 = \frac{c}{c_0} - 1 \tag{16}$$

Table 3. Refined values of the atomic fractional coordinates ($\times 10^4$) for the monoclinic β-phase (space group $C2/m$). The data obtained from C2 are shown in the upper section of the table, and the data from HRPD are shown in the lower section. For Na(3) errors range from 1×10^{-2} to 6×10^{-2} as $T \rightarrow T_c$. For all other atoms the errors are lower, ranging from 1×10^{-4} to 8×10^{-3}.

	Na(3)		C		O(1)			O(2)	
T (K)	x	z	x	z	x	y	z	x	z
605	1739	7509	1626	2475	1034	2976	2828	2924	1825
625	1737	7569	1635	2504	1025	2966	2783	2919	1838
645	1744	7517	1635	2507	1016	2997	2807	2918	1908
664	1698	7511	1643	2535	1017	3003	2798	2891	1899
684	1737	7411	1629	2536	1032	2985	2782	2926	1990
699	1752	7647	1628	2501	1026	3020	2797	2903	2001
703	1830	7630	1554	2450	994	3018	2746	2900	2047
718	1719	7599	1633	2449	1045	3053	2744	2902	2024
723	1758	7612	1596	2436	1015	3012	2725	2903	2127
737	1700	7672	1759	2506	1123	2943	2659	2897	2018
741	1710	7633	1589	2438	952	3019	2647	2893	2334
746	1708	7556	1574	2383	969	3047	2561	2896	2466
749	1740	7787	1779	2411	1129	3008	2598	2928	2115
751	1631	7557	1550	2422	820	3069	2410	2867	2243
611	1766	7536	1632	2481	1005	2930	2808	2957	1866
655	1724	7557	1580	2451	979	2975	2744	2916	1847
673	1661	7704	1646	2506	1034	2988	2825	2881	1727
699	1694	7617	1635	2546	1023	2970	2745	2950	1922
743	1550	7404	1593	2490	959	3021	2549	3083	2257

Table 4. Refined values of the cell parameters and atomic fractional coordinate x for the oxygen atom ($\times 10^4$) in the hexagonal α-phase (space group $P6_3/mmc$) using data obtained from C2. (The fractional coordinates of the oxygen atoms are $x, -x, \frac{1}{4}$; see table 1.) Errors are of the order of 6×10^{-4} Å for the lattice parameters and 6×10^{-4} for the oxygen positional parameters at all temperatures measured.

T (K)	a (Å)	c (Å)	x (oxygen)
756	5.207 84	6.454 03	7958
761	5.207 05	6.459 25	7958
765	5.206 92	6.465 71	7976
770	5.207 56	6.471 37	7979
775	5.207 49	6.476 89	7978
780	5.207 46	6.481 97	7979
800	5.208 73	6.503 00	7982
828	5.209 94	6.532 50	7982
876	5.210 95	6.581 20	7974
972	5.213 04	6.676 32	7964

$$\epsilon_5 = \frac{a \cos \beta^*}{a_0} \tag{17}$$

where a_0, b_0 and c_0 are the values based on the hexagonal phase extrapolated below the transition temperature ($a_0 = \sqrt{3} b_0$) assuming a linear temperature dependence, shown as the straight lines in figure 2. The temperature dependences of the spontaneous strain components

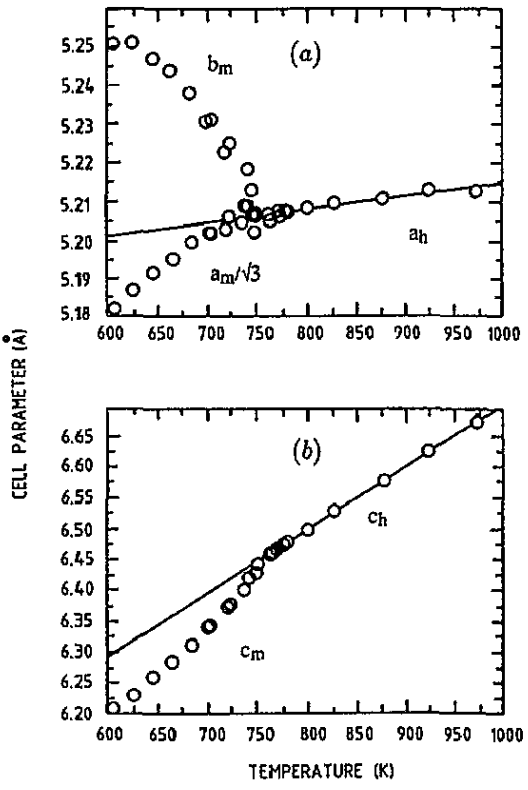

Figure 2. (*a*) Temperature dependence of the monoclinic unit cell parameters $a_m/\sqrt{3}$ and b_m, and the hexagonal unit cell parameter a_h. The straight line is the best fit to a_h extrapolated to lower temperatures, defined as b_0 in the text. (*b*) Temperature dependence of the monoclinic unit cell parameter c_m and the hexagonal unit cell parameter c_h. The straight line is the best fit to c_h extrapolated to lower temperatures, defined as c_0 in the text.

are shown in figure 3. The largest component is ϵ_5, which from symmetry is expected to behave as the order parameter. This shear strain is easily seen in figure 1. We have fitted the temperature dependence of ϵ_5 to a function of the form

$$\epsilon_5^2 = A((1 + B(T_c - T))^{1/2} - 1). \tag{18}$$

This equation follows from a Landau free energy function of the form

$$G(\epsilon_5) = \tfrac{1}{2}\eta_2(T - T_c)\epsilon_5^2 + \tfrac{1}{4}\eta_4\epsilon_5^4 + \tfrac{1}{6}\eta_6\epsilon_5^6. \tag{19}$$

It is not possible to isolate the values of η_2, η_4 and η_6 solely from the structural data, but it is possible to calculate the ratios between these parameters, as defined by A and B of equation (18). The fitted values are

$$A = \frac{\eta_4}{2\eta_6} = (2.72 \pm 0.05) \times 10^{-2} \tag{20}$$

$$B = \frac{4\eta_2\eta_6}{\eta_4^2} = (1.92 \pm 0.04) \times 10^{-2}\ \mathrm{K}^{-1} \tag{21}$$

$$T_c = 753.99 \pm 0.04\ \mathrm{K}. \tag{22}$$

The quartic coefficient η_4 is positive but the value of the sixth-order coefficient η_6 is significant. This suggests that the transition may be close to being first order. The fitted function is shown in figure 4. This graph shows a smooth extrapolation to zero, which is consistent with a continuous second-order phase transition.

The other strain components are coupled with ϵ_5 to quadratic and higher order. We have fitted them to polynomials of the form

$$\epsilon_j = a_2\epsilon_5^2 + a_4\epsilon_5^4. \tag{23}$$

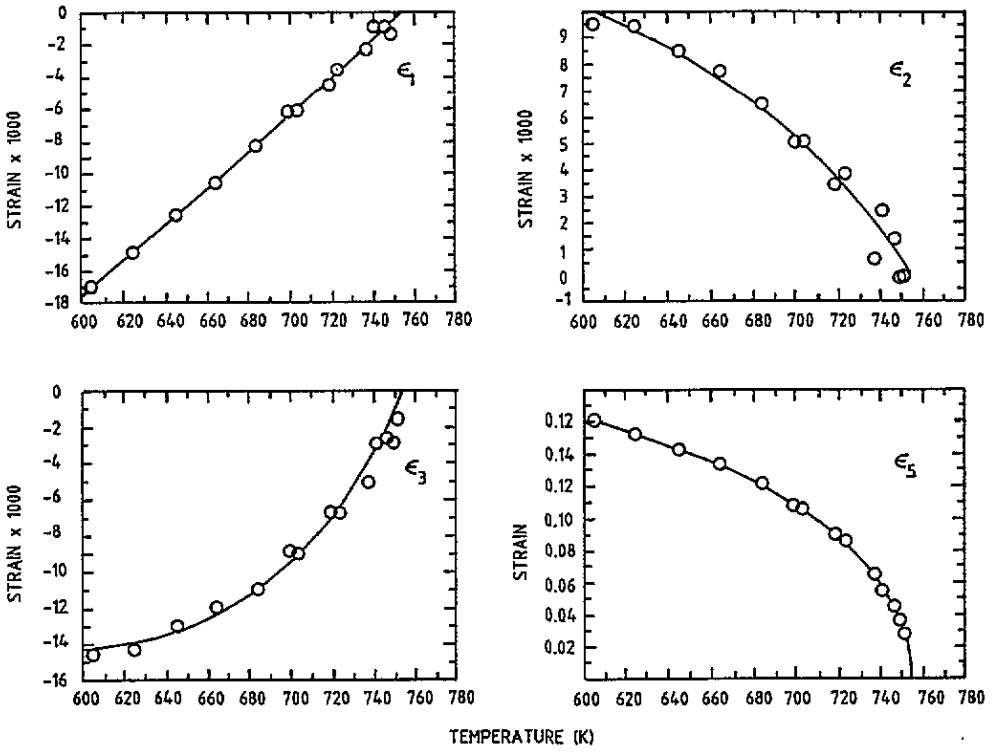

Figure 3. Temperature dependence of the spontaneous strain components ϵ_1, ϵ_2, ϵ_3 and ϵ_5. The curve for ϵ_5 is the result of fitting equation (18) to the data, and the curves for ϵ_1, ϵ_2 and ϵ_3 are the results of fitting to equations (23) and (18).

Table 5. Coefficients of the polynomial strain fits, as defined in equation (10).

Strain	a_2	a_4
ϵ_1	-0.46 ± 0.01	-6.9 ± 0.4
ϵ_2	-0.50 ± 0.01	-4.6 ± 0.5
ϵ_3	-1.01 ± 0.01	18.1 ± 0.7

The results are given in table 5, and are shown as the curves in figure 3.

4.3. Internal structural distortions

Detailed analysis of the temperature dependence of the atomic coordinates has shown that the significant atomic displacements apart from the shear strain are associated with the tilting of the CO_3 groups. This tilt is easily seen in figure 1. In figure 5 we show the temperature dependence of the tilt angle of the carbonate groups, ϕ_C. If all bond lengths remained unchanged as a function of temperature, ϕ_C should follow

$$\sin\phi_C = \frac{\sqrt{3}b_0}{2l_{O\text{-}O}}\epsilon_5 \tag{24}$$

where $l_{O\text{-}O}$ is the O–O distance within the CO_3 group. In fact equation (24) underestimates the size of ϕ_C. Experimentally we find that $\sin\phi_C \simeq (3.1 \pm 0.2)\epsilon_5$, whereas from the bond

lengths we would expect that $\sin\phi_C = 2.4\epsilon_5$. This suggests that there is some distortion of the NaO_6 octahedra, consistent with the observation that the c cell parameter changes quite markedly with temperature.

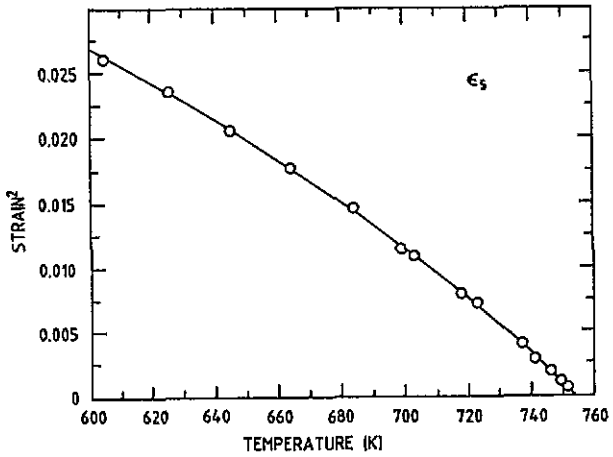

Figure 4. Temperature dependence of ϵ_5^2 with the curve fitted using equation (23).

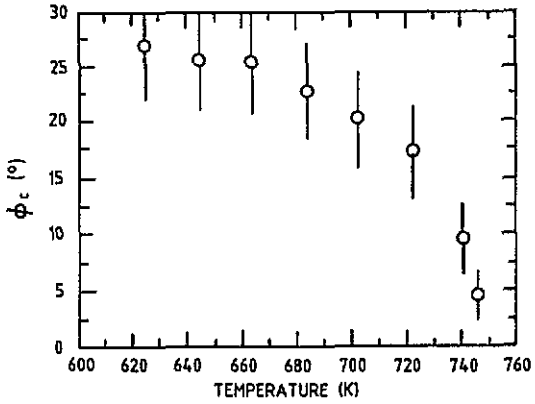

Figure 5. Temperature dependence of the CO_3 tilt angle, ϕ_C.

4.4. Temperature factors

In figure 6 we plot the inverse of the effective isotropic temperature factor of each atom as a function of temperature, averaging the results for the pairs of atoms that become equivalent in the hexagonal phase—we found no significant differences in the values for such pairs within the statistical errors. We again remind the reader that these temperature factors contain only the effects of the non-critical modes, and are described by equation (9). Values of temperature factors obtained from Rietveld refinement can be unreliable as a result of correlations within the refinements and the effects of neutron absorption, and we therefore do not attach quantitative significance to the absolute values we have obtained. However, the consistency from measurement to measurement shows that the qualitative trends in the temperature factors are reliable.

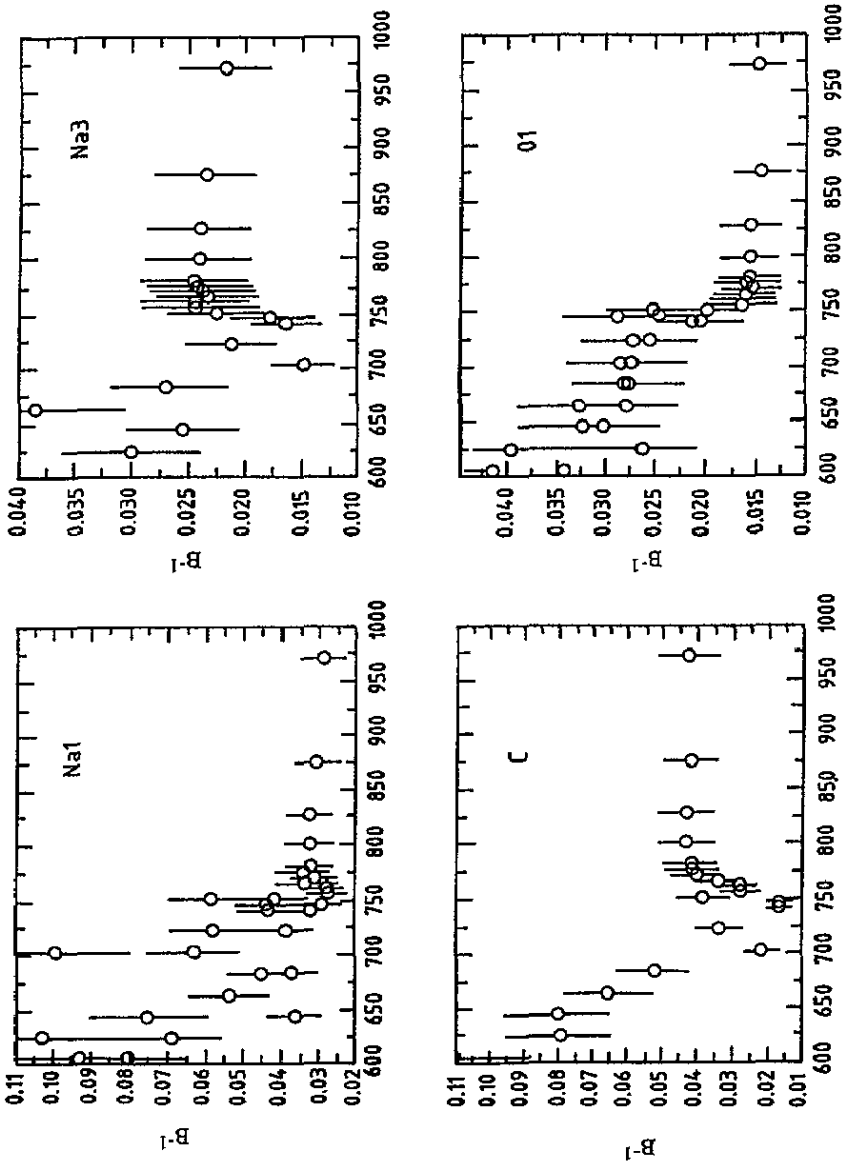

Figure 6. Temperature dependence of the inverse of the effective isotropic temperature factors ($1/B$) for Na(I) and the average of Na(1) and Na(2); Na(II) and Na(3); C; and O and the average of O(1) and O(2).

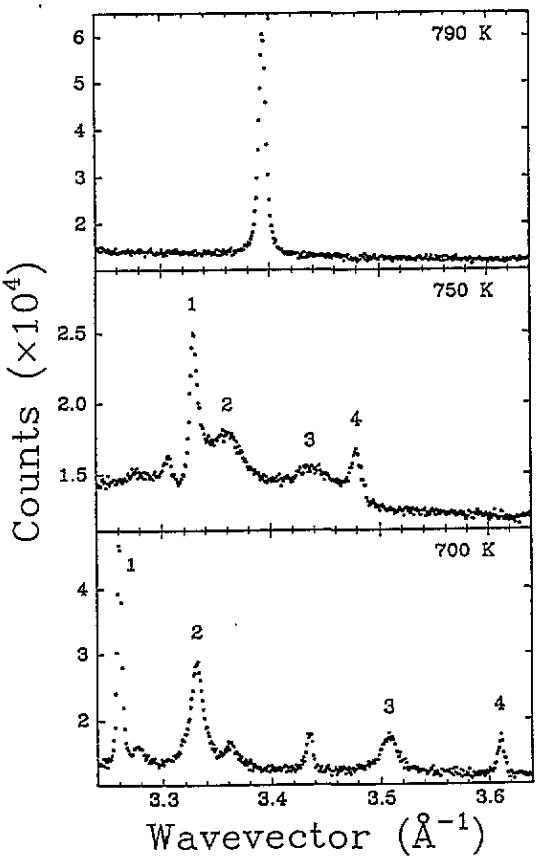

Figure 7. HRPD spectra at three temperatures showing the melting and recovery of Bragg peaks. The peak in the top spectrum is the hexagonal (2 0 2) Bragg reflection. The peaks marked as 1–4 in the middle and bottom spectra are from the monoclinic Bragg reflections $(\bar{4}\,0\,2)$, $(\bar{2}\,2\,2)$, (2 2 2) and (4 0 2) respectively.

The most striking behaviour is that of the carbon atom, whose temperature factor appears almost to diverge at the transition temperature. The octahedrally coordinated sodium atoms Na(1)/Na(2)/Na(I), and the oxygen atoms, show a less dramatic behaviour. Any divergence that may be present appears to be washed out and the temperature factors show more of a step function behaviour across T_c. We note that this change may arise from parameter correlations that are different in the refinements of the monoclinic and hexagonal structures. The temperature factor of Na(3)/Na(II) is large at all temperatures, as expected from the fact that it occupies a cavity larger than its ionic radius, but the temperature factor increases significantly at the transition temperature.

5. Discussion of the structural aspects of the phase transition

Our measurements and analysis presented in the previous section have shown that the α–β phase transition in sodium carbonate is completely described by a coupled spontaneous shear strain ϵ_5 and rotation of the carbonate groups, with additional strains coupled to higher order. We have found no evidence for any discontinuity at the transition temperature, and our fitted functional form for the temperature dependence of ϵ_5 within the framework of Landau

theory is consistent with a second-order phase transition. Weak logarithmic corrections to the temperature dependence of the order parameter of the familiar second-order, $m = 1$ ferroelastic transition are expected for the case of the $m = 2$ ferroelastic material [3, 6, 7]. We find no evidence of these from our data in the temperature range measured. This indicates that either their magnitude is either extremely weak and/or they only become apparent over a very small temperature range near T_c.

There is often an ambiguity in the question of the driving mechanism of any ferroelastic phase transition. If there is a linear coupling between the spontaneous shear strain and another order parameter, necessarily an optic mode distortion, then the corresponding elastic constant (in this case C_{44}) will automatically fall to zero at the transition temperature. Thus we are faced with the question of whether the acoustic instability is the driving mechanism for the phase transition or whether it simply follows an optic instability. In the case of sodium carbonate we have previously been able to answer this question unambiguously, and we found that the transition is driven by the C_{44} acoustic instability [19]. Our argument rests on what we call a *rigid-bond model* (RBM), which is a generalization of the *rigid-unit-mode model* that has been successfully applied to the study of phase transitions in silicates and other network solids [19, 20, 21, 22, 23]. In the RBM we assume that all nearest-neighbour contacts are perfectly rigid—this is the limit that the longitudinal force constants for nearest-neighbour contacts are much larger than the transverse force constants—and we search for any low-energy distortions that can occur within the RBM constraints. Our search takes the form of a lattice dynamics calculation for the hexagonal phase, with strong harmonic nearest-neighbour interactions, and three body interactions to preserve the shapes of the NaO_6 octahedra and carbonate groups. We exclude any long-range forces and we did not include the weakly bound Na(II) ion. The results of this calculation showed that the C_{44} transverse acoustic modes are soft for all wave vectors in the a^*–b^* plane, and that the optic mode that gives rise to the rotations of the carbonate groups is not a low-energy mode. The ability of the columns of NaO_6 octahedra to move up and down with respect to nearest-neighbour columns, being loosely hinged by the shared carbonate groups, reflects a soft shear mode, as anticipated by De Wolff and Tuinstra [1]. On the other hand, for the carbonate rotations to form a low-energy optic mode requires that there should be a way of decoupling this motion from the slower shear mode. The structure of sodium carbonate does not allow this possibility, as indicated by the RBM calculations. Thus we conclude that for sodium carbonate the primary instability is the C_{44} shear mode, and the carbonate rotations simply follow rather than drive the shear strain.

The importance of this result is that it demonstrates that sodium carbonate is a proper $m = 2$ ferroelastic, and is therefore the first continuous example of such a transition. It also demonstrates that the lattice melting effect is a direct consequence of the dimensionality of the order parameter.

6. Observation of the effects of lattice melting

6.1. Qualitative observations

The lattice melting in Na_2CO_3 produces a striking effect upon the powder diffraction spectrum, as seen in figure 7. Spectra obtained on HRPD are shown for temperatures above, just below and well below T_c. The Bragg peak in the hexagonal structure is (2 0 2), which in cooling into the monoclinic phase splits into the $(\bar{4}\,0\,2)$, $(\bar{2}\,2\,2)$, (2 2 2) and (4 0 2) reflections. On cooling towards T_c the intensity of the Bragg peak decreases, and the intensity of the broader diffuse scattering increases, until at T_c the Bragg peak has completely vanished.

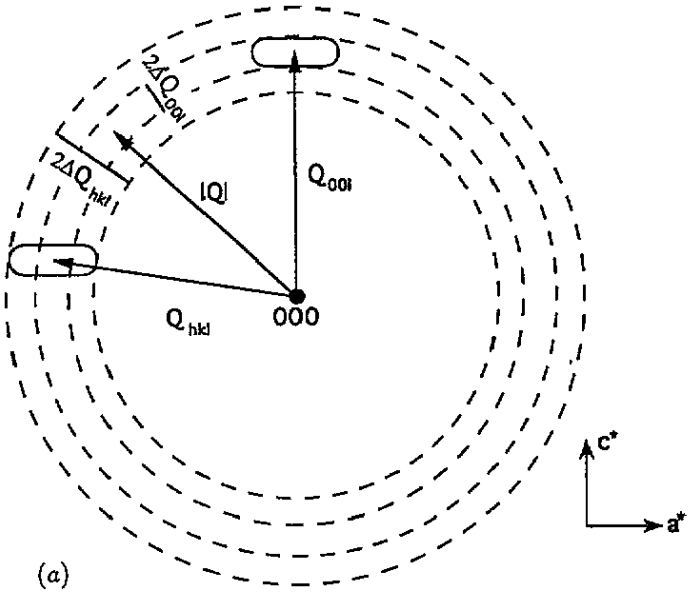

Figure 8. (*a*) Schematic diagram of the a^*–c^* reciprocal lattice net of Na_2CO_3 near T_c. All reciprocal lattice points with a component in c^* are broadened into discs in a^*–b^* due to the condensation of the transverse acoustic soft modes, which have wave-vectors in this plane and eigenvectors along c^*. Two reciprocal lattice points with the same $|Q|$ are shown: one ($Q_{00\ell}$) along c^* and one ($Q_{hk\ell}$) with a large component in the a^*–b^* plane. The four dotted circles are of radii fixed by the minimum and maximum $|Q|$ at which the reflection conditions for both reciprocal lattice discs could be satisfied. The widths of these minima and maxima about the mean $|Q|$ are $2\,\Delta Q_{00\ell}$ and $2\,\Delta Q_{hk\ell}$. (*b*) Schematic diagram for the case of constant-wavelength powder diffraction. The rings are now uniform distributions of the two reflections due to the powder averaging of all the reflections at all orientations with respect to the incident beam. The Ewald sphere of radius $2\pi/\lambda$ intersects both these $|Q|$ reflections, and the diffracted beams exit at 2θ to the incident beam. The inherent line width in 2θ (ignoring instrumental contributions) reflects the size and shape of the reciprocal lattice disc. Reflections with a large component in the a^*–b^* plane such as $hk\ell$ show a strong broadening, whereas reflections with $|Q|$ normal to the plane of softening see only the intrinsic, unbroadened line width.

The Bragg peaks reappear on cooling below T_c.

This lattice melting can be seen in figure 1 of De Wolff and Tuinstra [1], which shows a Guinier–Lenné photograph of sodium carbonate taken over a wide range of temperatures. Close to the monoclinic–hexagonal phase transition the traces of the Bragg peaks become blurred (apart from the (0 0 2) reflection). In particular, the effect shown in figure 7 of the present paper is clearly seen in the Guinier–Lenné photograph. In the figure caption that accompanies the Guinier–Lenné photograph in [1] the blurring is explained as vertical smearing due to the camera slit height, and whilst this is doubtless a contributary factor, the comparison with our figure 7 shows that this is not the sole explanation!

6.2. Lineshape analysis

We have already noted that the soft acoustic modes that produce the diffuse scattering are the transverse acoustic phonons with wave vectors in the a^*–b^* plane and eigenvectors parallel to [0 0 1]. In reciprocal space the diffuse scattering is in the shape of discs perpendicular

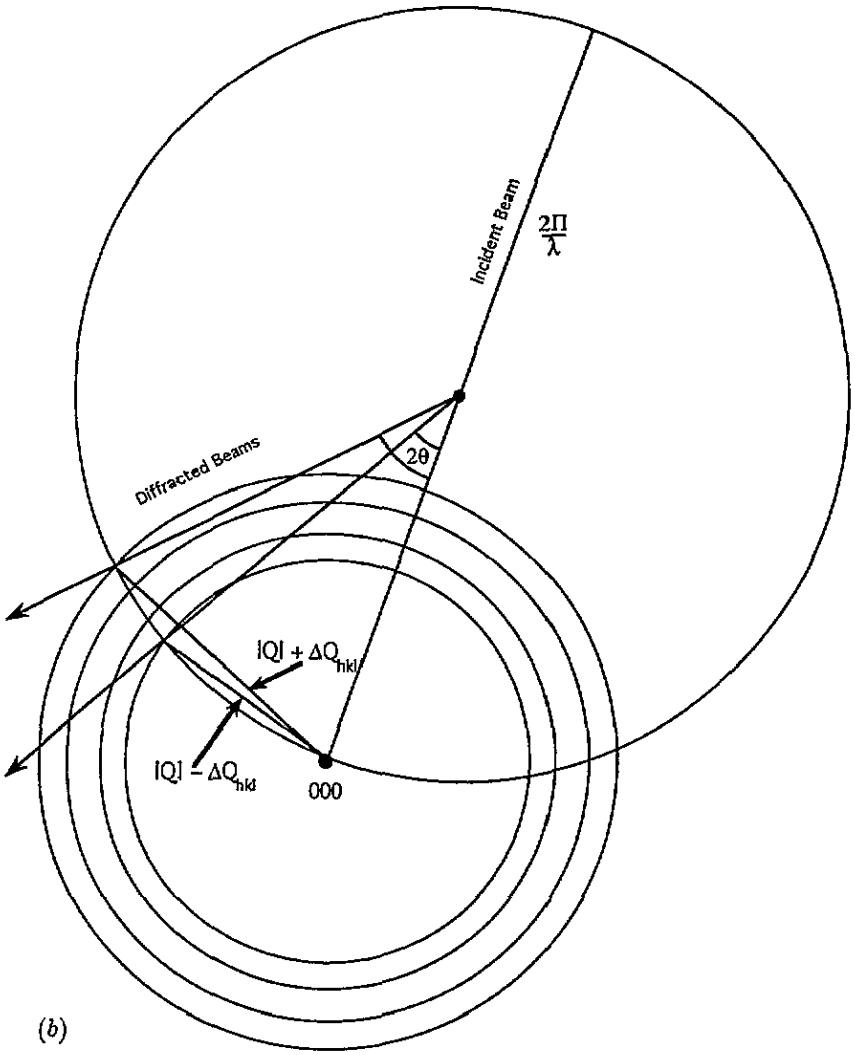

Figure 8. (Continued)

to [0 0 1] centred at the reciprocal lattice vectors with $\ell \neq 0$. A schematic view of an $h0\ell$ reciprocal lattice section is depicted in figure 8(*a*). The condition depending on ℓ arises from the fact that the scattering intensity is determined by $\boldsymbol{Q} \cdot \boldsymbol{e}$, where $\boldsymbol{Q}$ is the scattering vector and $\boldsymbol{e}$ is a vector along the direction of atomic motion. Since $\boldsymbol{e}$ is along [0 0 1], the diffuse scattering is only observed if there is a component of $\boldsymbol{Q}$ along the same direction. In a powder diffraction experiment, the reciprocal lattice is at all orientations with respect to the incident beam. This is depicted schematically in figure 8(*b*). The broadening effect at $T \approx T_c$, due to the shape of the reciprocal lattice 'discs', is preserved in a powder diffraction experiment. For reflections of the form $(0\,0\,\ell)$, $\boldsymbol{Q}_{00\ell}$ is normal to the discs and so no broadening is seen. For reflections of the form $(h\,k\,0)$ $\boldsymbol{Q} \cdot \boldsymbol{e}$ is zero and again broadening is not observed. However, for all other reflections $(h\,k\,\ell)$ not subject to these conditions considerable broadening is observed. The strongest peaks of diffuse scattering were observed at the (1 0 1), (2 0 1), (3 0 1), (2 0 2), (3 1 2), (1 0 3) and (2 0 3) reciprocal

lattice vectors. The widths of the peaks in the diffraction pattern were significantly broader than the instrumental resolution.

Mayer and Cowley [5] have shown that at T_c, when the Bragg component is zero, the diffuse scattering profile should have a power law lineshape. However, at temperatures away from T_c, when the Bragg intensities are no longer zero, there is no theoretical prediction for the lineshape of the diffuse scattering. We found that within the accuracy of the data the profiles of the diffuse scattering can be represented by the function

$$I(Q) = I_{(h\,k\,\ell)} \exp(-\left|Q - Q_{(h\,k\,\ell)}\right| / \kappa_{(h\,k\,\ell)}) \tag{25}$$

where $Q = |Q|$, $Q_{(h\,k\,\ell)}$ is the scattering vector for the Bragg reflection $(h\,k\,\ell)$ and $\kappa_{(h\,k\,\ell)}$ gives the width of the diffuse scattering. This profile function was convoluted with the Gaussian experimental resolution functions for each $(h\,k\,\ell)$, which were determined from the high-temperature diffraction patterns. Other functions we tested, including Lorentzian functions, were found to give an equally good representation of the diffuse scattering peaks, but Gaussian profiles were clearly not appropriate.

For each peak, $\kappa_{(h\,k\,\ell)}$ was determined at 756 K, where no Bragg component was observed, and then left fixed in the analysis of the scattering at higher temperatures. When the value of $\kappa_{(h\,k\,\ell)}$ was fitted at higher temperatures, where a significant Bragg component is also present, it was found not to vary outside the limits of the errors. A linear background was included, and the Bragg peaks were fitted using the profile of the resolution function determined at high temperatures. In general the fits gave values of $\chi^2 \simeq 1.0$, apart from the (1 0 1) peak where some trouble was encountered with the background owing to the proximity of the strong diffraction peak from the furnace. This treatment allowed us to extract the temperature dependence of the relative contributions of the Bragg scattering and the diffuse scattering. Owing to the large number of overlapping peaks in the monoclinic phase, especially close to T_c, most of our analysis was carried out on the data from the high-temperature hexagonal phase. Only one peak, (1 0 1), was analysed completely above and below T_c.

6.3. Results

Results of the fitting procedure for the (1 0 1), (2 0 2) and (3 1 2) peaks are shown in figure 9 for the data at 756 K, which is extremely close to T_c. At this temperature, no Bragg contribution was observable, and the fitted curves shown in the diagram solely represent the exponential profile convoluted with the resolution function. The (1 0 1) and (3 1 2) peaks have, respectively, the minimum and maximum values of the scattering vector that were analysed. The observed widths of the three peaks in the diagram are dependent on the resolution function and the changing effect of the powder average on the diffuse component.

In figure 10 we further illustrate the analysis procedure by showing the evolution of the scattered intensities for the (2 0 2) peak. As the temperature is increased above T_c, the diffuse component decreases rapidly in intensity and the width of the total scattering at the (2 0 2) position decreases towards the pure Bragg width given by the resolution function. At 799 K , it can be seen that the intensity of the diffuse component is very small compared to that of the Bragg part.

In figure 11 we show the integrated intensities of the Bragg and diffuse components of the (1 0 1), (2 0 2) and (1 0 3) peaks as a function of temperature. These three peaks were chosen since they illustrate most clearly the effect of increasing ℓ, which is discussed in the next paragraph. The intensity of the Bragg component of each peak falls to zero on approaching T_c, while the intensity of the diffuse component reaches its maximum at

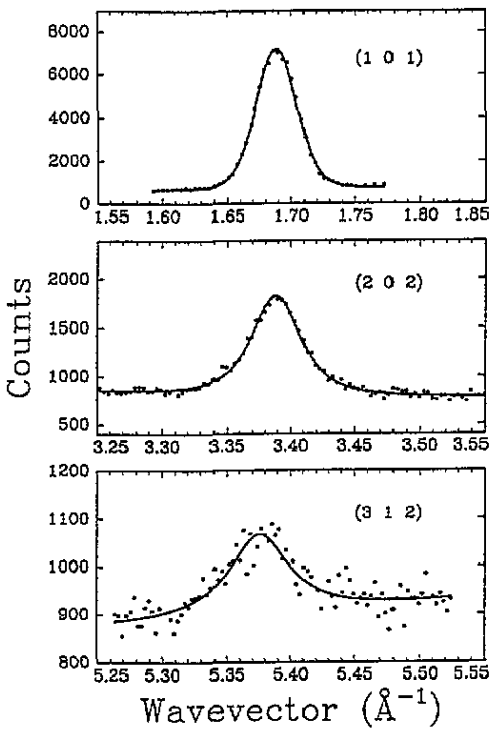

Figure 9. The (101), (202) and (312) peaks at 756 K, which is one degree above T_c. The fitted curves represent the pure diffuse scattering; no Bragg component is present.

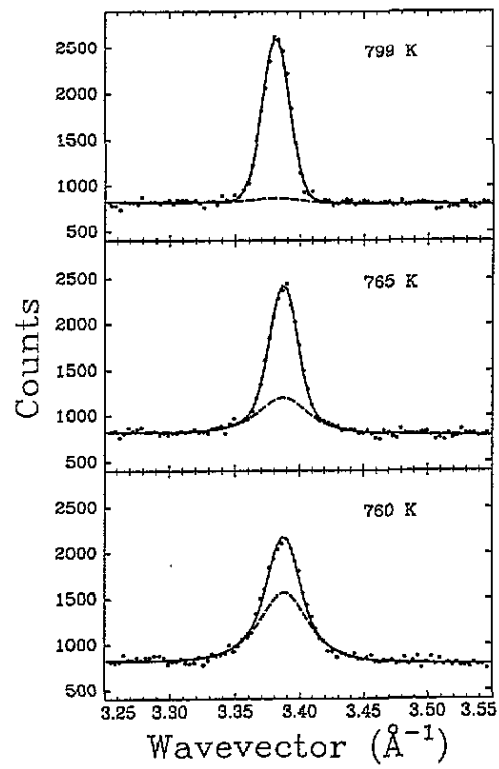

Figure 10. The temperature evolution of the line profile of the (202) peak above T_c. The broken line shows the exponential component, and the full line shows the complete analysed profile with the Bragg component included.

this point. The total intensity associated with each Bragg position remains approximately constant with temperature, as shown in figure 11 even though the process which occurs is in effect that of a delta function being replaced by a broad peak. This is the experimental support for the derivation of equation (12).

At 756 K , which is the closest temperature to T_c for which we have data, the spectra were fitted extremely well in all cases with just the diffuse component, as shown in figure 9. Any attempt to include the Bragg component into the fitting procedure at this temperature always led to it having negligible intensity, and this was found to be the case for all of the seven peaks which were analysed. Therefore, within the experimental resolution, the Bragg intensity at this temperature is vanishingly small or zero. We may then conclude that the mean squared atomic displacements diverge completely along the crystallographic [0 0 1] direction, and that long-range order is lost. Complete lattice melting is accomplished at this point.

Since there are relatively few overlapping peaks below T_c around the hexagonal (1 0 1) position in Na_2CO_3, a partial analysis of the diffuse and Bragg intensities associated with this reflection is possible. In figure 12 we show the data from figure 11 for the (1 0 1) peak around the transition, together with data points representing this partial analysis for one

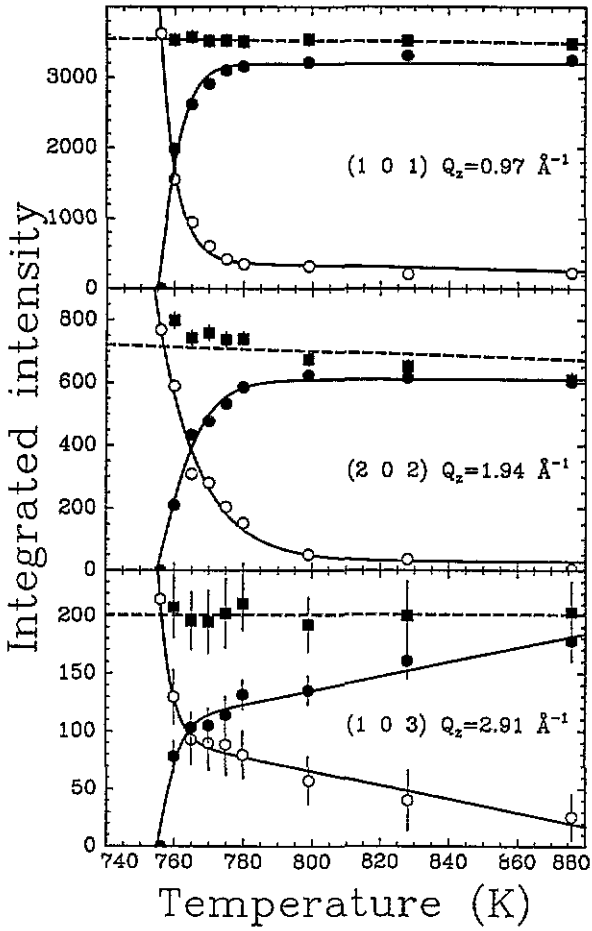

Figure 11. Temperature dependence of the diffuse scattering (open circles) and Bragg scattering (full circles) intensities for (1 0 1), (2 0 2) and (1 0 3) in the hexagonal phase. The closed squares represent the total integrated scattering (diffuse + Bragg) and show that to first approximation this is constant through the transition. The curves represent guides to the eye, and error bars are shown where the error exceeds the size of the data point.

temperature below T_c. The recovery of the Bragg component on cooling below T_c that is seen in this figure is consistent with the situation shown in figure 7.

Returning to figure 11, it can be seen that the behaviours of the Bragg and diffuse components are systematically different for each of the three peaks, which have different values of Q_z ($= 2\pi\ell/c$), the component of the scattering vector that is parallel to c^*. The changes in the Bragg and diffuse scattering components occur over a smaller range of temperatures the smaller the value of Q_z. This simply reflects the fact that the changes are associated with the divergence of the temperature factors, since the Bragg intensities with larger values of Q_z will be more sensitive to the mean square atomic displacements along [0 0 1]. Thus the divergence of the temperature factors associated with the lattice melting will be observed further from T_c in the reflections with larger values of Q_z. We have calculated an approximate temperature dependence of the part of the B_{33}^{A} temperature factor (i.e. the part of B_{33} that arises from the soft acoustic modes) from the three reflections

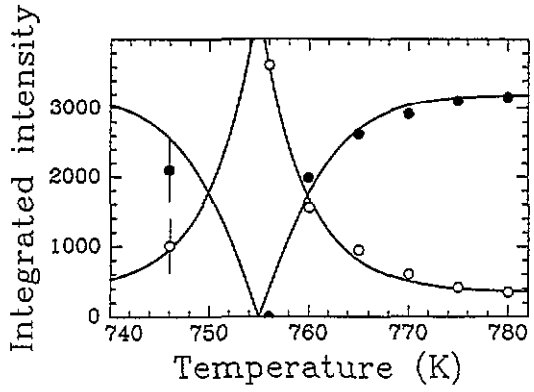

Figure 12. As for figure 11 for the (1 0 1) peak showing data below T_c.

shown in figure 11 using equation (13) and noting that

$$B_{33}^{A} = W^{A}/\ell^2. \tag{26}$$

Within error the temperature dependence of B_{33}^{A} should be the same for each reflection, given that the effect of the acoustic modes is to give each atom the same displacement. The temperature dependence of B_{33}^{A} is shown in figure 13, and the divergence on cooling towards T_c is clear. Further detailed analysis of these data is not practical since the accuracy is not good enough, and is worse in the important limits where $I_{\text{Bragg}} \gg I_{\text{Diffuse}}$ and $I_{\text{Bragg}} \ll I_{\text{Diffuse}}$.

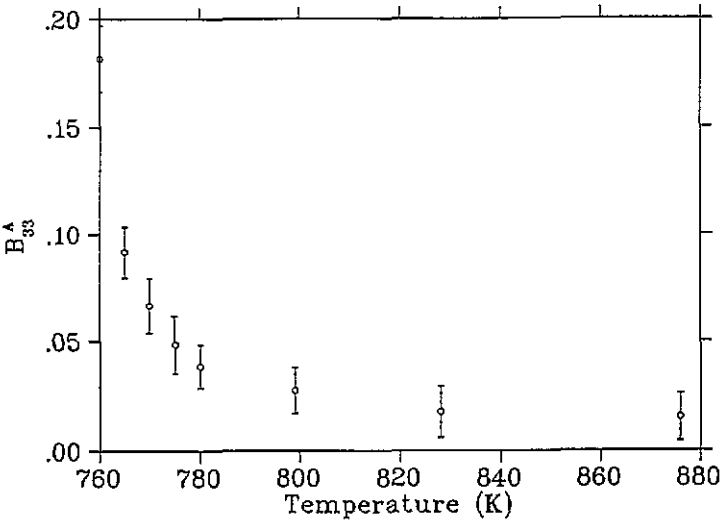

Figure 13. Temperature dependence of B_{33}^{A}.

Mayer and Cowley [5] have shown that at T_c the expected line profile of the diffuse scattering is proportional to $|Q - Q_{(hk\ell)}|^{-a}$, where the exponent a is dependent on Q_z^2. The numerical solutions to the complicated expressions indicate that, in a single-crystal experiment, the square root of the diffuse scattering width, $\Gamma_{(hk\ell)}^{1/2}$, should be roughly proportional to Q_z. We have calculated $\Gamma_{(hk\ell)}$, from our values of $\kappa_{(hk\ell)}$, by effectively reversing the powder average. In figure 14 we show that the expected approximate

proportionality of $\Gamma^{1/2}_{(hk\ell)}$ to Q_z holds. This result provides some validation of the Mayer–Cowley profiles.

Finally we compare our results with those from the single-crystal studies of the second-order phase transition in $(KBr)_{0.35}(KCN)_{0.65}$ [9], which we believe to be the only other system where similar effects have been observed. In this case it was found that at T_c the diffuse intensity dominates, but in contrast to our observations in Na_2CO_3 a residual Bragg component remained. This is believed to be due to the random defect fields present in these mixed systems, which tend to preserve long-range order [10]. Thus the ferroelastic phase transition in Na_2CO_3 is the first example where complete lattice melting has been observed.

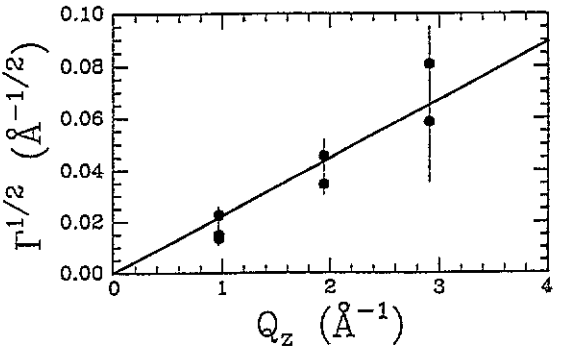

Figure 14. The dependence of $\Gamma^{1/2}_{(k\,k\,\ell)}$ on Q_z determined at 756 K. The straight line is the result of a least-squares fit through the origin.

7. Conclusions

We have presented experimental results for the crystallographic aspects of the ferroelastic phase transition in sodium carbonate with higher temperature resolution than before. We have demonstrated that the primary order parameter is the shear strain ϵ_5, and the other strains couple to ϵ_5 to higher order. The only significant rearrangement of the atomic positions is associated with the tilt of the carbonate groups, which act as hinges between the columns of NaO_6 octahedra. We have also demonstrated that the phase transition is second order with no significant non-classical critical behaviour. Our most striking results are the observations of the effects of lattice melting, associated with the divergence of the temperature factors predicted for continuous $m = 2$ ferroelastic phase transitions. We believe that our results are the first observations of complete lattice melting.

The fact that K_2CO_3 also displays lattice melting is a clear indication that it is the dimensionality of the order parameter that is responsible for the effect. Although the α-phases of K_2CO_3 and Na_2CO_3 are isostructural and the same order parameter is responsible for the two transitions, the detailed ferroic distortions differ and K_2CO_3 transforms into $C2/c$—an alternative basis of E_{1g}.

The neutron powder diffraction technique is necessarily limited in its scope. Having demonstrated in this study that sodium carbonate is an ideal prototype material for the analysis of $m = 2$ ferroelastic phase transitions, it would now be worthwhile attempting careful single-crystal diffraction studies of sodium carbonate at a number of temperatures in the vicinity of the phase transition in order to obtain accurate information about the line profiles and temperature factors.

Acknowledgments

We are grateful to Bill David (ISIS) for helpful discussions and for allowing us to use the REFINE program. Roger Cowley (Oxford) gave invaluable advice on the interpretation of the diffraction profiles. We are also grateful to Kevin Knight and Richard Ibberson (ISIS), who helped with the HRPD experiments, and Ron Donaberger (McMaster University) and Don Tennant (Chalk River), who helped with the C2 experiments. Travel funds for MTD and MJH were kindly provided by SERC (UK). MTD and MJH wish to thank the staff of Chalk River Laboratories for hospitality. MTD is grateful to Cambridge University for granting a year's study leave at Chalk River, during which this work was performed.

References

[1] de Wolff P M and Tuinstra F 1986 *Incommensurate Phases in Dielectrics* vol 2, ed R Blinc and A P Levanyuk (Amsterdam: North-Holland–Elsevier) p 253
[2] Harris M J and Salje E K H 1992 *J. Phys.: Condens. Matter* **4** 4399
[3] Cowley R A 1976 *Phys. Rev.* B **13** 4877
[4] Stokes H T and Hatch D M 1988 *Isotropy Subgroups of the 230 Crystallographic Space Groups* (Singapore: World Scientific)
[5] Mayer A P and Cowley R A 1988 *J. Phys. C: Solid State Phys.* **21** 4827
[6] Folk R, Iro R H and Schwabl F 1976 *Z. Phys.* B **25** 69
[7] Folk R, Iro R H and Schwabl F 1979 *Phys. Rev.* B **20** 1229
[8] Harris M J, Cowley R A, Swainson I P and Dove M T 1993 *Phys. Rev. Lett.* **71** 2939
[9] Loidl A, Knorr K, Rowe J M and McIntyre G J 1988 *Phys. Rev.* B **37** 389
[10] Mayer A P and Cowley R A 1988 *J. Phys. C: Solid State Phys.* **21** 4835
[11] Mikeska H-J and Schmidt H 1970 *J. Low Temp. Phys.* **2** 371
[12] Ibberson R M, David W I F and Knight K S 1992 *Rutherford Appleton Report* RAL-92-031
[13] Konyer N B and Root J H 1992 *AECL Report* RC-922
[14] Maciel A, Ryan J F and Walker P J 1981 *J. Phys. C: Solid State Phys.* **14** L509
[15] David W I F, Johnson M W, Knowles K J, Moreton-Smith C M, Crosbie G D, Campbell E P, Graham S P and Lyall J S 1986 *Rutherford Appleton Report* RAL-86-102
[16] David W I F, Ibberson R M and Matthewmann J C 1992 *Rutherford Appleton Report* RAL-92-032
[17] Brown P J and Matthewmann J C 1993 *Rutherford Appleton Report* RAL-93-009
[18] Rietveld H M 1969 *J. Appl. Crystallogr.* **2** 65
[19] Dove M T, Giddy A P and Heine V 1992 *Ferroelectrics* **136** 33
[20] Vallade M, Berge B and Dolino G 1992 *J. Physique* I **2** 1482
[21] Dove M T, Giddy A P and Heine V 1993 *Trans. Am. Crystallogr. Assoc.* **27** 65
[22] Tautz F S, Heine V, Dove M T and Chen X 1991 *Phys. Chem. Miner.* **18** 326
[23] Sollich P, Heine V and Dove M T 1994 *J. Phys.: Condens. Matter* **6** 3171